



HST/COS Observations of Quasar Outflows in the 500–1050 Å Rest Frame. I. The Most Energetic Outflows in the Universe and Other Discoveries

Nahum Arav¹ , Xinfeng Xu¹ , Timothy Miller¹ , Gerard A. Kriss² , and Rachel Plesha²

¹ Department of Physics, Virginia Tech, Blacksburg, VA 24061, USA; arav@vt.edu

² Space Telescope Science Institute, 3700 San Martin Drive, Baltimore, MD 21218, USA

Received 2019 June 27; revised 2019 December 30; accepted 2019 December 30; published 2020 March 16

Abstract

The *Hubble Space Telescope*/Cosmic Origins Spectrograph (COS) has opened a new discovery space for studying quasar absorption outflows and their contribution to active galactic nucleus (AGN) feedback. Specifically, COS provides high-quality far-ultraviolet (FUV) spectra covering the diagnostic-rich 500–1050 Å rest frame (hereafter, EUV500) of medium redshift objects. The quality and quantity of EUV500 diagnostic troughs allow us to probe the very high-ionization phase, which carries 90% or more of the outflowing material, as well as to determine the distance of most outflows from the central source (R). The first objective is impossible to achieve with ground-based spectra, and R can be measured in only $\sim 1\%$ of them. Here, we summarize the main results of the first dedicated survey of such outflows, including the following.

1. Measurements of the three most energetic outflows to date, which can be the main agents for AGN feedback processes in the environments of the host galaxies.
2. All the outflows have a very high-ionization component, similar to the one found in warm absorbers, which carries most of the outflow’s kinetic luminosity. This finding suggests that all the high-ionization outflows observed from the ground also have a similar undetected very high-ionization component.
3. Of the 13 studied EUV500 outflows, 9 have $100 < R < 2000$ parsecs, 2 have $5 < R < 20$ parsecs, 1 has $0.05 < R < 50$ parsecs, and in 1 case, R cannot be determined.
4. One of the outflows has the largest velocity shift (1550 km s^{-1}) and acceleration (1.5 cm s^{-2}) measured to date. This outflow is physically similar to the fast X-ray outflow detected in quasar PG 1211+143.

Unified Astronomy Thesaurus concepts: Active galaxies (17); Quasars (1319); Broad-absorption line quasar (183); Quasar absorption line spectroscopy (1317); Active galactic nuclei (16)

1. Introduction

Quasars show ubiquitous outflows ($\sim 20\%–50\%$ of all active galactic nuclei (AGN); e.g., Hewett & Foltz 2003; Dai et al. 2008; Ganguly & Brotherton 2008; Knigge et al. 2008), where blueshifted absorption lines, from ionized material, are attributed to subrelativistic ($\sim 10^3–10^4 \text{ km s}^{-1}$) mass ejection. These outflows are prime candidates for producing various AGN feedback processes: curtailing the growth of the host galaxy (e.g., Ciotti et al. 2009; Hopkins et al. 2009; Faucher-Giguère et al. 2012; Zubovas & King 2014; Schaye et al. 2015; Choi et al. 2017; Peirani et al. 2017), explaining the relationship between the masses of the central black hole and the galaxy’s bulge (e.g., Silk & Rees 1998; Blandford & Begelman 2004; Hopkins et al. 2009; Ostriker et al. 2010; Dubois et al. 2014; Rosas-Guevara et al. 2015; Volonteri et al. 2016; Anglés-Alcázar et al. 2017; Yuan et al. 2018), and intercluster medium (ICM) and intergalactic medium (IGM) chemical enrichment (e.g., Scannapieco & Oh 2004; Khalatyan et al. 2008; Tornatore et al. 2010; Barai et al. 2011; Taylor & Kobayashi 2015; Thompson et al. 2015). Theoretical models indicate that the kinetic luminosity (\dot{E}_k) must exceed either 0.5% (Hopkins & Elvis 2010) or 5% (Scannapieco & Oh 2004) of the quasar’s Eddington luminosity (L_{Edd}) for strong AGN feedback to occur; for a more detailed treatment, see Harrison et al. (2018).

In this paper, we concentrate on the common outflows seen in the rest-frame ultraviolet (UV) portion of the quasar spectra, whose troughs arise from ionized material. We note that AGN outflows are also detected in different phases (e.g., molecular;

see Cicone et al. 2018), as well as in optical emission lines (e.g., Zakamska & Greene 2014) and X-ray (e.g., Behar et al. 2017). Hereafter, we use the term “quasar outflows” in the narrow sense of rest-frame UV absorption outflows.

A few of the more important empirical questions regarding quasar outflows are:

1. What is their origin and acceleration mechanism?
2. What is the connection between the outflow and other parts of the AGN phenomenon: accretion disk, broad emission line region, narrow emission line region?
3. Are the outflows the main agent for the quasar mode of AGN feedback?

To advance our understanding on these questions, it is necessary to determine the outflows’ distances from the central source (R), their mass outflow rate (\dot{M}), and \dot{E}_k .

The large majority of quasar outflows show absorption troughs from only high-ionization species (e.g., C IV and Si IV), and there are more than 10,000 ground-based spectra of such outflows. However, almost all of these only cover rest-frame wavelengths longer than 1050 Å, where it is very rare to find diagnostic troughs that allow us to measure the distance of the outflow from the central source (R) and none for measuring its total hydrogen column density (N_{H}). The 500–1050 Å rest-frame region (hereafter EUV500) contains an order of magnitude more diagnostic troughs (see Figure 1). These include troughs from very high-ionization (VHI) species (ions with an ionization potential (IP) above 100 eV: e.g., Ne VIII, Na IX, Mg X, and Si XII) whose ionization phase carries most of

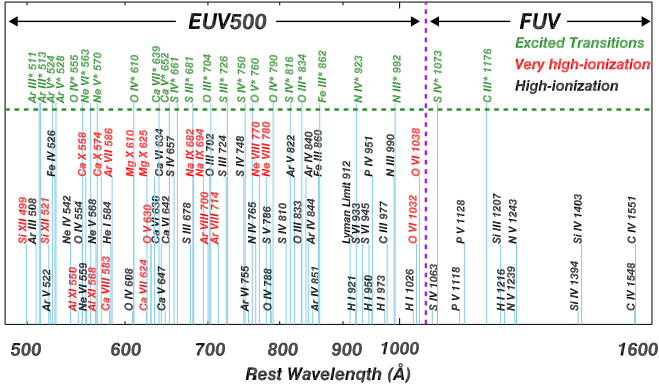


Figure 1. Comparison between the diagnostic power of the EUV500 and the $\lambda_{\text{rest}} > 1050$ Å (FUV) spectral regions. We show ionic transitions that are observed as absorption troughs in quasar outflows. No troughs from VHI species exist in the FUV, and, therefore, 90% or more of the outflow’s column density is unobservable. In contrast, the EUV500 contains detected outflow troughs from VHI species associated with the 19 transitions shown in red, which arise from 13 different ions (and this is not a complete list). In green, we show transitions from excited states. For high-ionization outflows, only two multiplets produce detected troughs from excited states at $\lambda_{\text{rest}} > 1050$ Å. Such detections are quite rare and are difficult to analyze (see Section 5.1). In contrast, for the EUV500, we show a representative sample of 22 transitions from excited states that are expected to produce outflow troughs. We detected such troughs from 16 of these transitions.

the outflowing N_{H} , (e.g., Arav et al. 2013) and troughs that allow us to determine R , which when combined with N_{H} , yields \dot{E}_k . We elaborate on the comparison between diagnostic power of the EUV500 and the $\lambda_{\text{rest}} > 1050$ Å spectral-regions in Section 5.1 (see also Figure 1).

From the ground, the EUV500 is accessible for quasars at redshift $z \gtrsim 3$ –4. Unfortunately, the Ly α forest at these redshifts is too thick to allow a meaningful outflow analysis. From space, using the Cosmic Origins Spectrograph (COS; Green et al. 2012), the *Hubble Space Telescope* (HST) can observe quasars at the $0.5 < z < 1.5$ range with sufficient signal-to-noise ratio (S/N) and spectral resolution to extract outflow science. In Arav et al. (2013), we analyzed COS EUV500 observations of the outflows seen in quasar HE 0238-1904 and found that more than 90% of the outflows’ column density—and, therefore, \dot{E}_k —resided in the VHI phase of these outflows.

In order to realize the science potential of EUV500 data for quasar outflows, we executed the first dedicated survey. This spectroscopic survey program (*HST* GO-14777, PI: N. Arav) observed 10 quasars with known EUV500 outflows at redshift $z \sim 1$. Each object was observed for four orbits, two each with COS gratings G130M and G160M (the objects and their observations are listed in Table 1). From the 10 targeted objects, we published results for the lowest redshift 1 (where the highest ionization species detected is O VI; Miller et al. 2018).

Here (Paper I), we give a summary of our scientific results and discoveries for the four objects where the outflow data lend themselves to accurate physical analysis. We then discuss the importance of these findings to various aspects of quasar outflow research. Detailed analyses of these observed outflows are given in the following series of papers:

Paper II (Xu et al. 2020a) gives the full analysis for four outflows detected in SDSS J1042+1646, including the largest

\dot{E}_k (10^{47} erg s $^{-1}$) outflow measured to date at $R = 800$ pc and an outflow at $R = 15$ pc.

Paper III (Miller et al. 2020a) analyzes four outflows detected in 2MASS J1051+1247, which show remarkable similarities, are situated at $R \sim 400$ pc, and have a combined $\dot{E}_k = 10^{46}$ erg s $^{-1}$.

Paper IV (Xu et al. 2020b) presents the largest velocity shift and acceleration measured to date in a broad absorption line (BAL) outflow.

Paper V (Miller et al. 2020b) analyzes two outflows detected in PKS J0352–0711: one outflow at $R = 500$ pc and a second outflow at $R = 10$ pc that shows an IP-dependent velocity shift for troughs from different ions.

Paper VI (Xu et al. 2020c) analyzes two outflows detected in SDSS J0755+2306, including one at $R = 1600$ pc with $\dot{E}_k = 10^{46}$ erg s $^{-1}$.

In the remaining five objects, we found significant intervening absorption, including cases of partial Lyman limit systems, as well as cases of significant self-blending of outflow troughs. Since these are somewhat more challenging to analyze, we will present their results in Paper VII (T. R. Miller et al. 2020, in preparation).

This paper is organized as follows. Section 2 describes the observed sample. Section 3 gives an overview of how the scientific results are extracted from the data. Section 4 gives a summary of the results from these investigations. In Section 5, we discuss the importance of these findings to various aspects of quasar outflow research, including: the many advantages of studying quasar outflows using EUV500 data (Section 5.1); measuring the dominant VHI phase (VHP) of the outflow (Section 5.1.1); determining the total N_{H} and ionization structure of the outflows (Section 5.1.2); the outflow distance determinations (Section 5.1.3); abundance determinations (Section 5.1.4); a comparison with X-ray observations of Seyfert and quasar outflows (Section 5.2); a comparison with earlier EUV500 observations of quasar outflows (Section 5.3); and the BAL definition for the EUV500 (Section 5.4). We summarize the main findings in Section 6.

For our analysis, we adopt a cosmology with $h = 0.696$, $\Omega_m = 0.286$, and $\Omega_\Lambda = 0.714$ and use Ned Wright’s Javascript Cosmology Calculator website (Wright 2006).

2. The Observed Sample and Outflow Identification

2.1. The Observed Sample

Details about our targets, including the dates and exposure times for each quasar, are found in Table 1. Our objects were selected following an exhaustive search in the UV quasar archives of *HST* (<https://archive.stsci.edu/hst/>), where we looked at data from all three generations of UV spectrographs: faint object spectrograph (FOS), space telescope imaging spectrograph (STIS), and COS. Most of these quasar spectra come from programs whose primary intent was to probe the intervening absorption from the IGM, the circumgalactic medium (CGM), galaxy halos, or high-velocity clouds. For most of these programs, quasar outflow troughs are a contaminant, and, therefore, objects with known outflows were purposefully omitted from their samples. This explains the paucity of outflow targets in the *HST* archive.

The sample selection was as follows:

1. The redshift range was 0.5–1.5. At $z > 0.5$, the strong lines from O IV, N IV, and Ne VIII are in the observed band of *HST*; and at $z > 1.5$, the Ly α forest becomes

Table 1
Objects Observed in Program *HST* GO-14777

Object	Redshift	G130M Observation		G160M Observation		Publication	Identification Observation		
		Date	Exp ^a	Date	Exp ^a		Instrument	Date	Exp ^a
LBQS J1206+1052	0.396	2017 Jul 18	4320	2017 Jul 18	4640	Miller ^b	COS G130M	2010 May 8	4840
VV2006 J0755+2306	0.854	2017 Sep 18–19	3550	2017 Sep 18	4660	Paper VI	COS G140L	2010 Dec 20	900
2MASS J1436+0727	0.894	2017 Jul 17	4130	2017 Jul 17	4660	Paper VII	COS G140L	2011 May 11	900
VV2006 J1329+5405	0.950	2017 Sep 30	3690	2017 Sep 30	4660	Paper VII	COS G140L	2011 Feb 21	900
PKS J0352–0711	0.966	2017 Aug 5	4070	2017 Aug 5	4660	Paper V	FOS G270H	1993 Sep 26	560
SDSS J1042+1646	0.978	2017 Nov 13	3360	2017 Nov 13	4920	Papers II/IV	COS G140L	2011 Jun 15	900
7C J1631+3930	1.025	2017 May 13	4200	2017 May 14	5200	Paper VII	FOS G270H	1993 Jul 21	400
SDSS J0936+2005	1.183	2017 Nov 21	4360	2017 Nov 22	4660	Paper VII	COS G140L	2011 Feb 13	900
SDSS J1051+1247	1.283	2018 Jan 4	3460	2018 Jan 4	4640	Paper III	COS G130M	2013 May 17	10870
SDSS J1123+0137 ^c	1.472	2017 Nov 15	3870	2017 Nov 15–16	4660	Paper VII	COS G140L ^d	2014 Jun 19	4990

Notes.

^a Exposure time in seconds.

^b Miller et al. (2018).

^c Also known as UM 425.

^d Additional identification observations from: *HST* FOS G270H: 1994 November 8 1320 s, and SDSS: 2002 December 28 2700 s.

thick enough that blending with outflow troughs in these low S/N data becomes a significant concern.

2. A minimum continuum flux of $2 \times 10^{-15} \text{ erg cm}^{-2} \text{ s}^{-1} \text{ \AA}^{-1}$ to allow for a reliable analysis.
3. Trough selection for the objects observed with either COS G140L or G130M. We searched for at least two troughs at the same velocity. To minimize false positive detections of intervening systems, we required the troughs to be wider than 500 km s^{-1} at a residual intensity of $I = 0.9$. For spectra that covered $700 \text{ \AA} < \lambda_{\text{rest}} < 800 \text{ \AA}$, we searched for the strongest expected pairs of resonance lines from the high-ionization phase (HP), O IV 787 Å and N IV 765 Å, and/or the Ne VIII $\lambda\lambda 770, 780$ for the VHP. For higher redshift objects, we used the Mg X doublet for the VHP and O IV 608 Å and O V 630 Å for the HP. Our survey identified eight targets using this procedure.
4. Trough selection for the objects observed with FOS G270H. For objects at $0.5 < z < 1.5$, FOS G270H observations cover only some of the $880 \text{ \AA} < \lambda_{\text{rest}} < 2180 \text{ \AA}$ range. In these cases, we searched for at least two troughs at the same velocity from the “traditional” outflow trough transitions: O VI $\lambda\lambda 1031.93, 1037.62$, Ly α , N V $\lambda\lambda 1238.82, 1242.80$, Si IV $\lambda\lambda 1393.76, 1402.77$, and C IV $\lambda\lambda 1548.20, 1550.77$. After identifying candidates in this way, we checked that their *Galaxy Evolution Explorer* (GALEX) photometry in the far-ultraviolet (FUV) is equal to or above the equivalent flux stated in criterion 2 above. Our survey identified two targets using this procedure.

Selection criteria 3 and 4 prevented bias toward:

- (a) Either the HP or the VHPs as we chose objects that showed troughs from either phase.
- (b) Any particular R scale since we searched for only resonance lines.

2.2. Outflow Identification

We define an outflow by the following two criteria. (1) An absorption feature is at least 500 km s^{-1} in width at a residual

intensity of $I = 0.9$. This is similar to the definition of a mini-BAL (Hamann & Sabra 2004). Such a width will avoid the vast majority of absorption troughs due to the Milky Way interstellar medium (ISM) and any other intervening absorption systems (e.g., IGM) as these are considerably narrower. (2) We require at least two troughs from different transitions that are at the same velocity for an outflow identification.

We define an outflow system as either: (a) an outflow where the red side of at least one trough returns to $I = 1$ and where the blue side of at least one trough (not necessarily the same trough) returns to $I = 1$, or (b) an internal structure within a trough where the maximum separating I is at least 20% higher than the minima on both sides in at least one trough. An example of one outflow separated into four systems is shown in Figure 2. We label systems in ascending order of absolute velocity: S1, S2, etc.

3. Overview of Science Extraction

We reduced the data and estimated the errors following the same procedure described in Miller et al. (2018). Detailed analyses of the EUV500 observations from this program are given in Papers II–VII. Here, we give an overview of the process needed to extract the scientific results from these data. To this end, we use one outflow (S2 in SDSS J1051+1247; see Paper III) as an example.

3.1. Richness of Diagnostic Troughs

A portion of the data for SDSS J1051+1247 (COS G130M observations) is shown in the top panel of Figure 2, where we detect troughs from 10 transitions. These transitions include VHI species of Mg X, Al XI, and Si XII; excited state transitions from Ne V and Ne VI, which are used to determine R ; and troughs similar to the majority detected at $\lambda_{\text{rest}} > 1050 \text{ \AA}$ (i.e., from resonance transitions of high-ionization species, here O IV). In the full data set, which includes our COS G160M observations of this object, we detect troughs from 17 transitions.

Ionic column densities (N_{ion}) are extracted using standard techniques (see Section 3.1 in Paper III). On the bottom panel of Figure 2, we show a blown up of the Si XII, Ne V, and Mg X troughs, which are marked in red rectangles on the top panel,

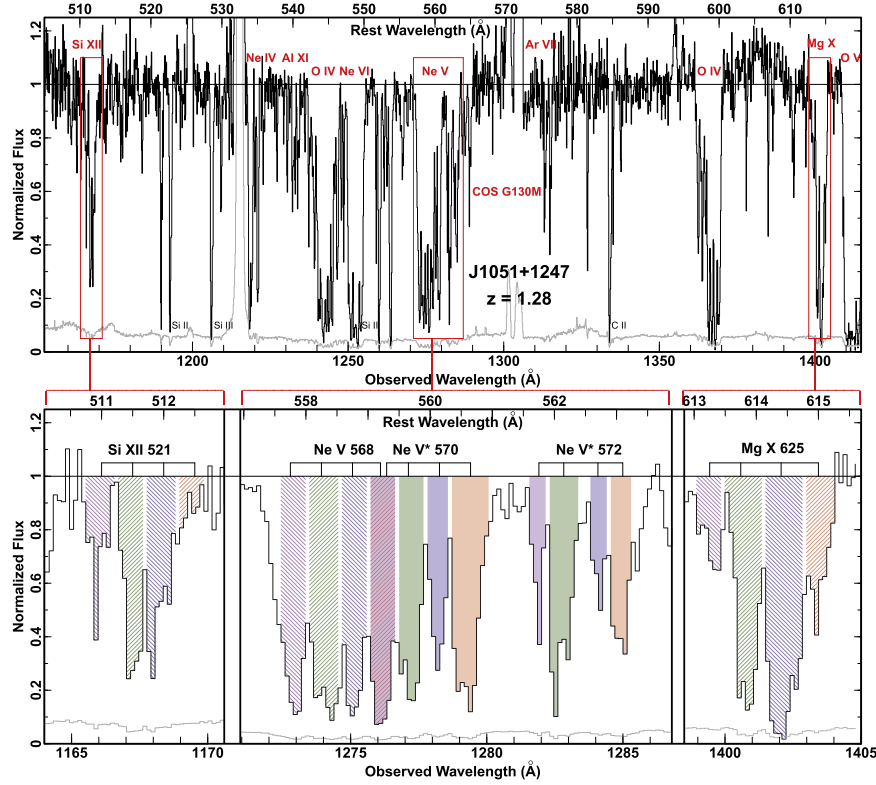


Figure 2. Top: a portion of the COS G130M data for SDSS J1051+1247, showing troughs from: VHI species (Mg X, Al XI and Si XII), excited transitions (O IV* and Ne V*), and high-ionization species (O IV). Bottom: a blow up of the Si XII, Ne V, and Mg X troughs, showing the four detected outflow systems, resonance troughs as hatched filled regions, and troughs from excited states as solid filled regions.

for the four detected outflow systems (S2 is marked with blue shading). The keys for determining the physical properties of the VHP of the outflow are the N_{ion} extracted from the Si XII and Mg X troughs, the Al XI trough (seen in the top panel of Figure 2), and the Na IX and Ne VIII troughs detected in the COS G160M data. Likewise, the keys for determining the electron number density (n_e) of the outflow (and therefore R) are the N_{ion} extracted from the troughs associated with the resonance transition Ne V 568 Å and the excited state transitions Ne V* 570 Å and Ne V* 572 Å (see Section 3.3 for elaboration).

3.2. Determining N_H and U_H

Ionization equilibrium in quasar outflows is dominated by photoionization, where the outflow is characterized by its ionization parameter (U_H) and total hydrogen column density (N_H). We run the spectral synthesis code Cloudy (version c17.00; Ferland et al. 2017) to generate grids of photoionization simulations (see Arav et al. 2013) to find the solution that best fits the measured N_{ion} . The multitude of detected troughs in the EUV500 give many N_{ion} constraints that yield reliable and over-constrained solutions (see Section 5.1.2). Figure 3 shows constraints only for S2, whose troughs are shown as the blue filled regions on the bottom panel of Figure 2. The data requires two (well-constrained) ionization phases (see Arav et al. 2013). We note that the N_H of the VHP is ~ 40 times larger than that of the HP, and they differ by a factor of 20 in their U_H values. Similar results are obtained for the other three outflow systems seen in SDSS J1051+1247 (see Paper III).

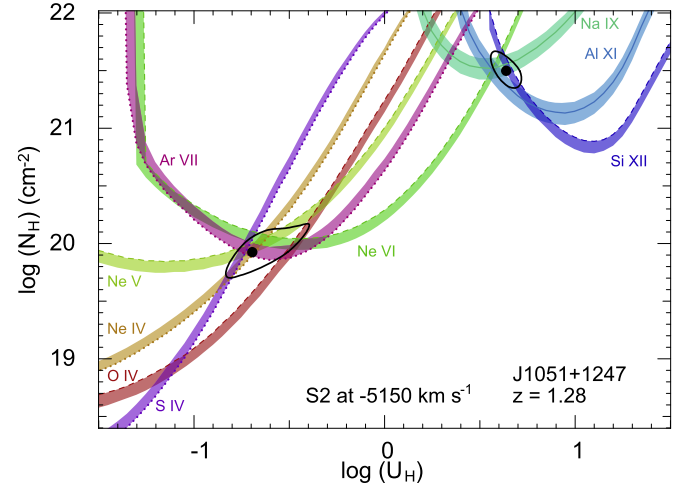


Figure 3. Photoionization grid models (based on Cloudy; Ferland et al. 2017) showing the outflow's ionization constraints. A solid contour represents the locus of N_H and U_H models that predict the observed N_{ion} . The bands on each side represent the 1σ uncertainties in the measurements. Dashed lines are for N_{ion} lower limits, allowing for the phase space above them, and, similarly, dotted lines are N_{ion} upper limits, allowing for the phase space below them. Here, we show the ionization solutions for the -5150 km s^{-1} outflow system (S2) seen in the COS data of SDSS J1051+1247 (portions of which are shown in Figure 2). The two solutions for each phase are marked by the black dots and are surrounded by 1σ confidence intervals (black contours).

3.3. Determining n_e and R

The most robust way for determining R for quasar absorption outflows is the use of troughs from ionic excited states (see Section 7.1 in Arav et al. 2018). The column density ratio

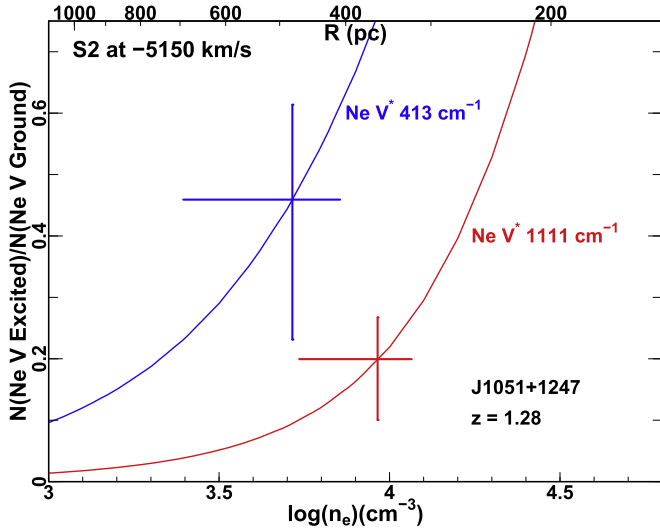


Figure 4. n_e and R diagnostics for S2 in SDSS J1051+1247: We first determine n_e by measuring the column density ratio between troughs from excited and ground state energy levels of a given ion. The theoretical curves for two Ne V excited states and the measurement of their N_{ion} ratios with respect to the resonance state are plotted. The top x-axis shows the derived R using Equation (1) and the U_{H} value of system 2.

between the excited and resonance states yields the electron number density (n_e). With the knowledge of n_e , we determine R from the value and definition of the ionization parameter (see Equation (13.6) in Osterbrock & Ferland 2006):

$$U_{\text{H}} \equiv \frac{Q_{\text{H}}}{4\pi R^2 n_{\text{H}} c}, \quad (1)$$

where n_{H} is the hydrogen number density with $n_{\text{H}} \simeq 0.8n_e$ for a highly ionized plasma, R is the distance of the outflow from the central source, c is the speed of light, and Q_{H} is the incident ionizing photon rate of hydrogen. A comparative discussion of all the methods (found in the literature) that are used to determine R is given in Arav et al. (2018)’s Section 7.1.

The EUV500 includes several transitions from excited states of abundant high-ionization species (e.g., O III, IV, and V; and Ne V and VI, see Figure 1), which produce troughs in most high-ionization outflows. Thus, n_e can be measured in the majority of EUV500 outflows and, in some instances, by more than one diagnostic, which makes the n_e determination more reliable.

The n_e measurements for S2 are based on the Ne V troughs seen on the bottom panel of Figure 2. The solid filled troughs are from the excited state transitions at 572.33 Å ($E_{\text{low}} = 1111 \text{ cm}^{-1}$) and 569.83 Å ($E_{\text{low}} = 413 \text{ cm}^{-1}$), where E_{low} is the lower energy level at which the electron absorbs the photon. The hatched filled troughs are from the resonance line at 568.41 Å ($E_{\text{low}} = 0$). We use the code CHIANTI (version 7.1.3; Dere et al. 1997; Landi et al. 2013) to calculate the theoretical N_{ion} ratios of the excited to the $E_{\text{low}} = 0$ states, as a function of n_e . The input temperature is the one determined by Cloudy for the lower ionization solution shown in Figure 3, which produces almost all the Ne V ions. Figure 4 shows these theoretical N_{ion} ratios, where the measured ratios with uncertainties for each level are overlaid on the theoretical curves, thus determining n_e .

For SDSS J1051+1247, $Q_{\text{H}} = 7.3 \times 10^{56} \text{ s}^{-1}$ (see Section 4.1 in Paper III). Using the n_e derived from Figure 4 and the U_{H} deduced from the HP solution (the VHP produces negligible

amounts of Ne V), we derive $R = 360^{+130}_{-100} \text{ pc}$ for S2 (see elaboration in Paper III).

3.4. Determining \dot{M} and \dot{E}_k of the Outflow

With the knowledge of N_{H} and R , the mass outflow rate (\dot{M}) and kinetic luminosity (\dot{E}_k) of the outflow can be determined from (for elaboration, see Section 2.1 in Arav et al. 2013)

$$\dot{M} \simeq 4\pi\Omega R N_{\text{H}} \mu m_{\text{p}} v \quad (2)$$

and

$$\dot{E}_k = \frac{1}{2} \dot{M} v^2 \simeq 2\pi\Omega R N_{\text{H}} \mu m_{\text{p}} v^3, \quad (3)$$

where Ω is the fraction of the total solid angle occupied by the outflow, m_{p} is the mass of the proton, $\mu \simeq 1.4$ is the mean molecular weight of the plasma per proton, and v is the velocity of the outflow. $\Omega = 0.40$ is estimated by the fraction of all quasars showing similar width outflows (see Section 4.1 in Paper III), and v is measured from the deepest portion of the outflow trough. We note that since in all our outflows $\Delta v/v < 0.1$ (where Δv is the width of the outflow), the exact position where v is measured in the outflow produces only small differences in the derived \dot{M} and \dot{E}_k .

Using the total measured N_{H} and the above R value, we obtain for S2 $\dot{E}_k \simeq 2.9 \times 10^{45} \text{ erg s}^{-1}$. The four outflow systems in SDSS J1051+1247 combined have $\dot{E}_k \simeq 8.8 \times 10^{45} \text{ erg s}^{-1}$, which is roughly 7% of its L_{Edd} . Therefore, the outflows in this object can be major contributors to AGN feedback mechanisms.

3.5. Volume Filling Factor

Kinematic similarities (both velocity centroid and width) between troughs from the HP and VHP are evidence that the two phases are cospatial. The volume filling factor, f_v , between the two phases is defined as the ratio of volumes between the HP and VHP (see Section 8.1 in Arav et al. 2013). For each phase, the volume is proportional to $N_{\text{H}}/n_{\text{H}}$, and the n_{H} ratio between the HP and the VHP is given by $U_{\text{H,VHP}}/U_{\text{H,HP}}$. Therefore,

$$f_v \equiv \frac{V_{\text{HP}}}{V_{\text{VHP}}} = \frac{N_{\text{H,HP}}}{N_{\text{H,VHP}}} \times \frac{U_{\text{H,HP}}}{U_{\text{H,VHP}}}. \quad (4)$$

For S2, we obtain $f_v = 0.001$.

4. Results

Table 2 shows all the derived parameters for the 13 outflows detected in the EUV500 observations of the four quasars discussed here. For the photoionization solutions, we systematically used the HE0238 SED (Arav et al. 2013). For SDSS J1042+1646 and SDSS J1051+1247, we used solar abundances. For PKS J0352–0711 and VV2006 J0755+2306, the photoionization solutions require roughly 5 times solar metallicity (see Papers V and VI). For comparison, we also show results for the previous largest \dot{E}_k outflows (Arav et al. 2013; Chamberlain et al. 2015). In this section, we elaborate about the major findings and their significance to quasar outflow research.

Table 2
Analysis Results^a

System	v^b (km s ⁻¹)	$\log(U_{\text{H,HP}})$ log	$\log(N_{\text{H,HP}})$ log(cm ⁻²)	$\log(n_e)$ log(cm ⁻³)	$\log(U_{\text{H,VHP}})$ log	$\log(N_{\text{H,VHP}})$ log(cm ⁻²)	$\log(f_v)^c$	R (pc)	\dot{M} (M_\odot yr ⁻¹)	$\log \dot{E}_k$ log(erg s ⁻¹)	$\dot{E}_k / L_{\text{Edd}}$ %
SDSS J1042+1646, $L_{\text{bol}} = 1.5 \times 10^{47}$ erg s ⁻¹											
1a	-4950	-1.0 ^{+0.2} _{-0.3}	20.4 ^{+0.4} _{-0.6}	3.7 ^{+0.2} _{-0.3}	0.4 ^{+0.2} _{-0.1}	22.4 ^{+0.2} _{-0.1}	-3.4 ^{+0.5} _{-0.7}	840 ⁺⁵⁰⁰ ₋₃₀₀	2800 ⁺²⁰⁰ ₋₈₀₀	46.4 ^{+0.1} _{-0.1}	10 ⁺³ ₋₂
1b	-5750	-0.9 ^{+0.2} _{-0.2}	20.5 ^{+0.4} _{-0.3}	3.8 ^{+0.2} _{-0.3}	0.5 ^{+0.2} _{-0.2}	22.5 ^{+0.3} _{-0.2}	-3.4 ^{+0.6} _{-0.5}	800 ⁺³⁰⁰ ₋₁₅₀₀	4300 ⁺¹²⁰⁰ ₋₁₅₀₀	46.7 ^{+0.2} _{-0.1}	20 ⁺¹⁴ ₋₄
2	-7500	-0.6 ^{+0.2} _{-0.1}	20.8 ^{+0.3} _{-0.3}	5.8 ^{+0.5} _{-0.3}	0.4 ^{+0.1} _{-0.1}	22.4 ^{+0.1} _{-0.1}	-2.6 ^{+0.4} _{-0.6}	15 ⁺⁸ ₋₈	81 ⁺²⁰ ₋₃₀	45.1 ^{+0.1} _{-0.2}	0.5 ^{+0.2} _{-0.2}
3	-9940	-0.7 ^{+0.1} _{-0.1}	20.7 ^{+0.2} _{-0.2}	...	0.1 ^{+0.1} _{-0.1}	21.5 ^{+0.1} _{-0.1}	-1.6 ^{+0.6} _{-0.3}
4	-21050	4.5-10.5	0.2-0.9	20.8-22.2	...	0.05-50	0.07-140	43.0-46.3	0.004-8
2MASS J1051+1247, $L_{\text{bol}} = 1.3 \times 10^{47}$ erg s ⁻¹											
1	-4900	-0.8 ^{+0.3} _{-0.1}	20.3 ^{+0.4} _{-0.2}	3.9 ^{+0.1} _{-0.3}	0.3 ^{+0.5} _{-0.1}	21.1 ^{+0.4} _{-0.6}	-1.9 ^{+0.8} _{-0.7}	460 ⁺²⁰⁰ ₋₁₃₀	180 ⁺³¹⁰ ₋₁₂₀	45.1 ^{+0.5} _{-0.5}	1.1 ^{+2.4} _{-0.8}
2	-5150	-0.7 ^{+0.3} _{-0.2}	19.9 ^{+0.2} _{-0.2}	4.0 ^{+0.1} _{-0.2}	0.6 ^{+0.1} _{-0.1}	21.5 ^{+0.2} _{-0.2}	-2.9 ^{+0.4} _{-0.4}	360 ⁺¹³⁰ ₋₁₀₀	350 ⁺²⁶⁰ ₋₁₇₀	45.5 ^{+0.2} _{-0.3}	2.3 ^{+3.1} _{-1.4}
3	-5350	-0.3 ^{+0.2} _{-0.6}	20.6 ^{+0.5} _{-0.5}	4.2 ^{+0.1} _{-0.4}	0.6 ^{+0.1} _{-0.1}	21.5 ^{+0.2} _{-0.3}	-1.8 ^{+0.6} _{-0.8}	180 ⁺²²⁰ ₋₅₀	180 ⁺³²⁰ ₋₉₀	45.2 ^{+0.5} _{-0.5}	1.3 ^{+3.0} _{-0.8}
4	-5650	-0.8 ^{+0.3} _{-0.1}	19.8 ^{+0.2} _{-0.2}	3.9 ^{+0.1} _{-0.2}	0.6 ^{+0.1} _{-0.1}	21.3 ^{+0.3} _{-0.3}	-2.9 ^{+0.5} _{-0.4}	460 ⁺¹⁶⁰ ₋₁₄₀	300 ⁺³⁸⁰ ₋₁₇₀	45.5 ^{+0.3} _{-0.4}	2.3 ^{+4.4} _{-1.5}
PKS J0352-0711, ^d $L_{\text{bol}} = 5.5 \times 10^{46}$ erg s ⁻¹											
1	-1950	-0.7 ^{+0.3} _{-0.3}	19.1 ^{+0.5} _{-0.9}	3.2 ^{+0.2} _{-0.1}	0.2 ^{+0.6} _{-0.1}	20.3 ^{+0.4} _{-0.6}	-2.1 ^{+0.8} _{-1.2}	520 ⁺³⁰⁰ ₋₁₅₀	11 ⁺²² ₋₈	43.1 ^{+0.5} _{-0.6}	0.01 ^{+0.04} _{-0.01}
2	-3150	-1.0 ^{+0.2} _{-0.5}	20.5 ^{+0.4} _{-0.7}	5.8 ^{+0.8} _{-0.3}	0.3 ^{+0.4} _{-0.2}	21.6 ^{+0.3} _{-0.3}	-2.4 ^{+0.6} _{-0.3}	9 ⁺⁵ ₋₅	7.5 ⁺⁹ ₋₃	43.4 ^{+0.3} _{-0.3}	0.02 ^{+0.06} _{-0.01}
SDSS J0755+2306, ^d $L_{\text{bol}} = 4.4 \times 10^{46}$ erg s ⁻¹											
1	-5520	-1.2 ^{+0.3} _{-0.2}	19.9 ^{+0.6} _{-0.2}	4.3 ^{+0.2} _{-0.2}	>0.1	>20.7	<-2.1	270 ⁺¹⁰⁰ ₋₉₀	>21	>44.3	>0.2
2	-9660	-1.6 ^{+0.6} _{-0.5}	19.5 ^{+0.7} _{-0.6}	3.1 ^{+0.8} _{-0.5}	>0.1	>21.4	<-3.3	1600 ⁺²⁰⁰⁰ ₋₁₁₀₀	>450	>46.1	>12.5
Comparison to Other Energetic Outflows:											
HE 0238-1904 ^{a,e}	-5000	-2.4 ^{+2.0} _{-0.1}	17.5 ^{+2.0} _{-0.1}	3.7 ^{+0.1} _{-0.1}	0.5 ^{+0.2} _{-0.1}	20.8 ^{+0.1} _{-0.2}	-6.2 ^{+2.8} _{-0.3}	3000 ⁺⁹⁰⁰ ₋₂₈₀₀	160 ⁺⁸⁰ ₋₁₅₀	45.7 ^{+0.2} _{-1.2}	4 ⁺² ₋₃
J0831+0354 ^{a,f}	-10800	-0.2 ^{+0.4} _{-0.5}	22.4 ^{+0.5} _{-0.5}	4.4 ^{+0.3} _{-0.2}	80 ⁺²⁷ ₋₁₈	230 ⁺³³⁰ ₋₁₃₀	45.9 ^{+0.4} _{-0.3}	8 ⁺¹¹ ₋₄

Notes.

^a The results for the last two entries are from Arav et al. (2013) (HE 0238-1904) and Chamberlain et al. (2015) (SDSS J0831+0354).

^b The velocity centroid of each outflow system. Conservative uncertainties are ± 40 km s⁻¹ for all outflows.

^c The volume filling factor of the outflow's HP relative to the VHI phase.

^d The photoionization solutions assume roughly 5 times solar metallicity (see Paper V).

^e For quasar HE 0238-1904, $L_{\text{bol}} = 1.5 \times 10^{47}$ erg s⁻¹.

^f For quasar SDSS J0831+0354, $L_{\text{bol}} = 6.2 \times 10^{46}$ erg s⁻¹.

4.1. The Prevalence of the VHP and Its Importance to Outflow Research

Arav et al. (2013) showed the existence of two ionization phases in a quasar outflow. One is the HP that is detected in all outflows observed at $\lambda_{\text{rest}} > 1050 \text{ \AA}$ (the large majority of ground-based observations), and the other is the VHP evident by troughs from VHI species (e.g., Ne VIII, Mg X, and Si XII) that can be detected only in the EUV500. All 13 outflows we discuss here have a VHP, and our analysis yields the following insights:

1. The VHP carries between 5 and 100 times larger N_{H} (and, therefore, \dot{E}_k , see Equation (3)) than the HP (see Table 2). This demonstrates that (a) quantitative studies of the outflows' origin and their effects on the host galaxy's environment are crucially dependent on the parameters of the VHP, and (b) attempting to deduce the VHP N_{H} from the N_{H} of the HP using a single scale factor would yield inaccurate results since there is a large spread (factor of 20) of the N_{H} ratio between the phases.
2. Of the 13 outflows, 12 have both an HP and a VHP (S4 in SDSS J1042+1646 shows only a VHP) and have detected O IV troughs. In a given outflow, the expected optical depth of the O IV troughs at 609 \AA ($\tau_{\text{O IV}609}$) and/or 788 \AA ($\tau_{\text{O IV}788}$) should be similar to that of the C IV 1549 \AA trough ($\tau_{\text{C IV}1549}$). This is because, for example,

$$\begin{aligned} \frac{\tau_{\text{O IV}788}}{\tau_{\text{C IV}1549}} &= \left[\frac{N_{\text{O IV}}}{N_{\text{C IV}}} \right] \left[\frac{f_{\text{O IV}788} 788 \text{ \AA}}{f_{\text{C IV}1549} 1549 \text{ \AA}} \right] \\ &= \left[\frac{\text{O}}{\text{C}} \frac{F_{\text{O IV}}(U_{\text{H}})}{F_{\text{C IV}}(U_{\text{H}})} \right] [0.29] = 0.61 \frac{F_{\text{O IV}}(U_{\text{H}})}{F_{\text{C IV}}(U_{\text{H}})} \sim 1 \end{aligned} \quad (5)$$

where $N_{\text{O IV}}$ and $N_{\text{C IV}}$ are the ionic column densities for O IV and C IV, respectively; f is the oscillator strength; O/C is the abundance ratio of oxygen to carbon (2.1 for solar metallicity); and $F(U_{\text{H}})$ is the ratio of the ion's number density to the total number density for the element (all ionization stages). Since $F_{\text{O IV}}(U_{\text{H}})/F_{\text{C IV}}(U_{\text{H}}) = 1.6$ near the peak $F(U_{\text{H}})$ for both ions, the expected value for $\tau_{\text{O IV}788}/\tau_{\text{C IV}1549} \simeq 0.61 \times 1.6 = 1.0$. Therefore, all 12 outflows should have a detectable C IV 1549 \AA trough, labeling them as high-ionization outflows if observed only at $\lambda_{\text{rest}} > 1050 \text{ \AA}$.

It is also probable that the large majority of high-ionization outflows observed at $\lambda_{\text{rest}} > 1050 \text{ \AA}$ also have a VHP since, (a) we detect only 1 of 13 outflows that has only a VHP; and (b) O VI 1034 \AA troughs are detected in almost all the ground-based spectra of outflows that cover their expected wavelength range. Since O VI is a VHI (IP of 138 eV), its appearance strongly suggest the existence of a VHP.

4.2. The Three Most Energetic Outflows to Date

Even with errors taken into account, outflows 1a and 1b in SDSS J1042+1646 individually have an \dot{E}_k larger than the previously published record (Chamberlain et al. 2015; see the last entry in Table 2). Outflow 2 in SDSS J0755+2306 also has a larger \dot{E}_k nominally, but within the errors, the value is similar to the previous record. A similar situation occurs for the

combined \dot{E}_k of the four outflows seen in 2MASS J1051+1247, which are probably physically related (see Paper III). Therefore, we have three outflows (the combined 1a and 1b in SDSS J1042+1646; the combined 1, 2, 3. and 4 outflow in 2MASS J1051+1247; and outflow 2 in SDSS J0755+2306) whose \dot{E}_k exceeds or is equal to the largest \dot{E}_k value currently reported in the literature. This plethora of extremely energetic outflows stem from our ability to measure the VHP, which carries 80%–99% of the total N_{H} in our studied EUV500 outflows (see Table 2).

We note that the claim of the “most energetic outflows to date” extends to all quasar outflows where \dot{E}_k can be reliably determined (i.e., where R can be measured). This includes all outflow phases at any redshift.

4.3. Contribution to AGN Feedback

All three outflows described in Section 4.2 have a $\Gamma_{\text{Edd}} \equiv \dot{E}_k/L_{\text{Edd}}$ larger than the 5% conservative threshold needed for an outflow to produce major AGN feedback (Scannapieco & Oh 2004). Outflows 2 and 4 in SDSS J1042+1646, and outflow 1 in SDSS J0755+2306 have Γ_{Edd} values close to 0.5%, which is the lower threshold for producing significant AGN feedback (Hopkins & Elvis 2010). The two independent outflows in PKS J0352–0711 have $\Gamma_{\text{Edd}} \simeq 0.03\%$, which is too small to produce significant AGN feedback.

Therefore, roughly half of the outflows discussed here have a high enough Γ_{Edd} value to produce major AGN feedback processes. Although our sample is small and heterogeneous (see Section 2.1), this finding suggests that a large fraction of quasar outflows are capable of producing AGN feedback once the N_{H} of their VHP is taken into account.

4.4. Distance from the Ionizing Source (R)

Table 2 shows that 9 of the 13 studied EUV500 outflows have $100 < R < 2000 \text{ pc}$, 2 have $5 < R < 20 \text{ pc}$, 1 has $0.05 < R < 50 \text{ pc}$, and for 1 outflow, R cannot be determined. This spread of R values support the findings from ground-based observations of S IV troughs that about half of all quasar outflows are situated at $R > 100 \text{ pc}$ (Arav et al. 2018; Xu et al. 2019).

4.5. The Largest Quasar Outflow Acceleration

Outflow 4 in SDSS J1042+1646 (classified as a BAL outflow) has the largest velocity shift (1550 km s^{-1}) and average acceleration (1.5 cm s^{-2}) measured to date (see Paper IV). These findings are based on two epochs of COS observations, 2011 and 2017, which are separated by 3.2 yr in the quasar's rest frame. Between these two epochs, the outflow's velocity changed from $-19,500 \text{ km s}^{-1}$ to $-21,050 \text{ km s}^{-1}$. A few points to note about this finding:

1. This is the first time where a quasar outflow acceleration is observed in more than one trough (four troughs show the same velocity shift).
2. This is the first time where we have R constraints for an accelerating outflow. Together with future *HST*/COS observations, these R constraints will allow us to test outflow acceleration models (e.g., Murray & Chiang 1997) in a more substantial way than was previously possible.

3. The systematic investigation of C IV BAL acceleration/deceleration reported in Grier et al. (2016) shows a low detection rate of accelerating outflows (2 out of 140 quasars), where their 2 acceleration candidates show velocity shifts of up to $\sim 900 \text{ km s}^{-1}$ over rest-frame times of 3–5 yr. Due to this low detection rate, our finding would have been unusual if observed solely in the C IV trough (which is in a wavelength range that our observations do not cover). However, as noted in Section 4.1, this EUV500 outflow is the only one where we detect troughs only from the VHP (and, therefore, we do not expect to detect a C IV trough associated with it). The 12 outflows with an HP do not show any velocity shift over two COS epochs that are separated by a similar time interval to those of SDSS J1042+1646 (see Papers II, III, V, and VI). The nondetection in 12 cases is consistent with the Grier et al. (2016) detection rate of 2 in 140 cases. Therefore, we speculate that perhaps pure VHP outflows show a higher rate of detectable acceleration since they might be situated closer to the central source (in this case, $0.05 < R < 50$ parsecs). This may also explain the high acceleration value for this outflow.

4.5.1. Similarity with the PG 1211+143 X-Ray Outflow

Outflow S4 has a similar velocity to the X-ray outflow seen in PG 1211+143 ($-17,300 \text{ km s}^{-1}$), which is detected by troughs from Ne X–Ly α , Mg XII–Ly α , Si XIII–He α , and Si XIV–Ly α using *Chandra* observations (Danehkar et al. 2018; see also Pounds et al. 2016a, 2016b for detection of similar troughs using *XMM-Newton* Reflection Grating Spectrometer data). This X-ray absorber in PG 1211+143 is well fitted with $\log(N_{\text{H}}) \sim 21.5$ and $\log(\xi) \sim 2.9$, where ξ is the X-ray ionization parameter. For the HE 0238 SED, $\log(U_{\text{H}}) = \log(\xi) - 1.3$. The UV counterpart of this X-ray outflow has been detected in *HST*/COS observations, which yields a broad Ly α absorption feature at $v = -17,000 \text{ km s}^{-1}$ ($-0.056c$; Kriss et al. 2018). We compare the v , N_{H} , and U_{H} values between the X-ray outflow in PG 1211+143 and outflow S4 in Table 3 of Paper IV. We conclude that our observations in the EUV500 band have probed an outflow with similar physical characteristics to the one observed in PG 1211+143.

4.6. IP-dependent Velocity Shift

Outflow 2 observed in PKS J0352–0711 (at $v \simeq -3150 \text{ km s}^{-1}$) shows a unique velocity centroid shift between associated troughs. Troughs from N III and O III have a velocity centroid at $v \simeq -3100 \text{ km s}^{-1}$. Troughs from higher IP species show a gradual velocity-centroid shift, whose magnitude is correlated with increasing IP, where troughs from the highest IP ions (Ne VIII and Na IX) have a velocity centroid at $v \simeq -3200 \text{ km s}^{-1}$.

5. Discussion

5.1. The Many Advantages of Studying Quasar Outflows Using EUV500 Data

Here, we detail the necessity of analyzing EUV500 observations and the advantages compared to ground-based data. The only disadvantage of such an analysis is programmatic: the need

for *HST* observations, which is a limited and highly sought after resource in many research fields.

5.1.1. Measuring the Dominant VHP of the Outflow

As detailed in Section 4.1, the VHP carries up to 99% of the column density and energy of the outflow. Clearly, a reliable physical study of the outflows requires measurements of the VHP phase. Ground-based observations can detect troughs from the O VI doublet around 1034 \AA , which is a VHI species. However, measurements of N_{ion} from O VI and lower ionization species do not require a VHP to fit the data. For example, Xu et al. (2018) measured $N_{\text{ion}}(\text{O VI})$, yet an ionization solution with only an HP fits the data well.

Therefore, measuring the VHP necessitates EUV500 data covering troughs from Ne VIII and higher ionization species (e.g., see Figure 3).

5.1.2. Determining the Total N_{H} and Ionization Structure of the Outflows

Outflow troughs are known to exhibit non-black saturation, where in extreme cases the real optical depth is a thousand times larger than the apparent optical depth (AOD) deduced from the depth of the trough (Borguet et al. 2012a). Not accounting for this possibility can lead to N_{H} values that are only a few percent of the actual one (Arav et al. 2015). Therefore, we usually treat the N_{ion} of the abundant species (H I, C IV, N V, and sometimes Si IV) as lower limits. Since these are the only troughs detected in the large majority of ground-based data, it is not possible to derive a U_{H} , N_{H} solution for these outflows.

In contrast, the EUV500 data show many more troughs from ions with a large range of ionic abundances. From such data we can extract: N_{ion} where we have indications that the trough is not saturated; lower limits for troughs thought to be saturated; and upper limits for non-existent troughs of a given species. We are conservative in our decision to adopt N_{ion} as measurements (see Section 3.1 in Paper III). However, the plethora of EUV500 troughs yield enough upper and lower limits to well-constrain both ionization phases of the outflow. Moreover, these limits are immune to saturation effects. Lower limits allow for the solution to be above the N_{ion} curve irrespective of the real N_{ion} , and upper limits of course do not suffer from saturation. Given enough constraints of both types, a well-confined solution can be reached.

As an example, in Figure 3, the photoionization solutions for the HP in this outflow is constrained only by N_{ion} upper and lower limits. However, the multitude of upper and lower limits tightly constrain the solution.

Therefore, it is relatively straightforward to determine the photoionization solutions for EUV500 outflows, whereas it is very challenging for the large majority of outflows with only ground-based spectra.

5.1.3. Outflow Distance Determinations

Most published R determinations (e.g., de Kool et al. 2001; Hamann et al. 2001; de Kool et al. 2002; Korista et al. 2008; Moe et al. 2009; Bautista et al. 2010; Dunn et al. 2010; Aoki et al. 2011; Lucy et al. 2014; Leighly et al. 2018) come from singly ionized species that have excited levels (mostly from Si II and Fe II). However, some 90% of quasar outflow spectra show absorption troughs only from higher ionization species.

Therefore, the applicability of R derived from Si II and Fe II to the majority of outflows is somewhat model-dependent (see the discussion in Section 1 of Dunn et al. 2012).

From the ground, the main high-ionization species with detected troughs arising from an excited state is S IV, which has resonance and excited level transitions at 1063 Å and 1072 Å, respectively (C III* is another option, but there are only a handful of spectra where it is detected). Published R determinations using S IV include Borguet et al. (2012b, 2013), Chamberlain et al. (2015), and Xu et al. (2018, 2019).

However, a few factors limit the use of S IV as an R diagnostic. (1) Due to the small oscillator strength of the transitions and the low abundance of S compared to C, these troughs are observed in only 10%–15% of the spectra that show C IV troughs (Arav et al. 2018). (2) The high redshift needed to shift the S IV trough into the ground-based spectral region does not allow the detection of these troughs in quasars at redshift smaller than 2–2.8 (depending on the spectrograph). (3) The thick Ly α forest at these redshifts complicate the detection and measurements of these troughs.

In contrast, the EUV500 covers many excited transitions from abundant species that produce outflow troughs (see Figures 1 and 2). Such usable troughs (allowing for an n_e determination) are detected in most such outflows (in 12 out of the 13 studied here). Furthermore, the Ly α contamination is much smaller in redshift 0.5–1.5 objects.

An alternative method for determining n_e is via a photo-ionization timescale analysis (this timescale is inversely proportional to the n_e of the outflow; see Arav et al. 2015). However, this method is both resource intensive (many observational epochs are needed) and is model-dependent (see the discussion in Section 7.1 of Arav et al. 2018).

5.1.4. Abundance Determinations

There are two advantages for attempting to determine abundances using EUV500 data:

1. High-ionization outflow data, covering $\lambda_{\text{rest}} > 1050$ Å, usually show troughs from only H, C, N, and Si (and in rare cases, P and S). In the EUV500, we detect troughs from H, N, O, Ne, Na, Mg, Al, Si, S, Ar, Ca, and Fe, allowing for the abundances of many more elements to be determined.
2. In the $\lambda_{\text{rest}} > 1050$ Å region, C and N show troughs from only one ion (Si has two), making an abundance determination highly uncertain. The standard method is to vary each abundance until all the N_{ion} curves yield the optimal solution on the $N_{\text{H}}, U_{\text{H}}$ parameter space. However this is more akin to assuming a set of abundances without any way to verify it. In the EUV500 we have several cases of troughs from different ions of the same element: for example, O III, IV, V, and VI; and Ne IV, V, VI, and VIII. Such occurrences yield abundance-independent U_{H} and N_{H} solutions (as they arise from the same element). The reliability of these solutions is higher as we do not have abundances as free parameters. Once we have confidence in the elemental solutions, making the solutions for different elements consistent would yield a better constrained set of abundances. In a future paper,

we will use these attributes to constrain the abundances of these EUV500 outflows.

5.2. Comparison with X-Ray Observations of Seyfert and Quasar Outflows

Spectroscopic X-ray observations of Seyfert outflows detect the so-called warm-absorbers. In all cases, the need for two or more ionization phases is evident (e.g., Netzer et al. 2003; Steenbrugge et al. 2005; Holczer et al. 2007; Kaastra et al. 2014; Behar et al. 2017). This is mainly due to the much larger spread in IP of the observed ionic species (e.g., O V (IP = 114 eV) to S XVI (IP = 3500 eV)). Unfortunately, in most cases the X-ray spectra lack the resolution to kinematically associate the warm absorber with the UV absorber seen in the same object.

The EUV500 data has both the S/N and spectral resolution to kinematically associate troughs from the VHP with troughs from the HP. Therefore, we are confident that both phases come from the same R , which validate our calculation methods for \dot{M} and \dot{E}_k . For elaborations of these issues, see the discussion in Section 8.1 of Arav et al. (2013).

5.3. Comparison with Earlier EUV500 Observations of Quasar Outflows

Observations of EUV500 quasar outflows predate *HST*. Pettini & Boksenberg (1986) observed BALQSO PG 0946+301 using the *IUE* satellite and identified EUV500 troughs from N IV, O IV, O V, and Ne VIII. Soon after that, *HST* was launched with 2 orders of magnitude higher sensitivity in the UV. Korista et al. (1992) used FOS to observe BALQSO 0226-1024. They measured N_{ion} for 14 ionic species from EUV500 troughs, but the measurements suffered from heavy trough blending as the full width of the outflow was 25,000 km s⁻¹. Telfer et al. (1998) observed the high-redshift BALQSO SBS 1542+541 using FOS, detected Si XII troughs, and made the first attempt to find the ionization solution using troughs from VHI species. Arav et al. (2001) published a similar ionization solution using STIS observations of PG 0946+301.

In hindsight, all of these early efforts suffered from similar limitations:

1. The targeted outflows had trough widths larger than 4000 km s⁻¹ (partially chosen because of the low spectral resolution of the spectrographs and the intent of observing BALs) and, therefore, suffered from considerable blending of troughs in the EUV500.
2. The resultant large uncertainties in the measured N_{ion} did not allow for the identification of two different ionization phases.
3. Troughs from excited ionic states were either not identified or too blended to measuring their N_{ion} (Arav et al. 1999), e.g., the O III* troughs detected in FOS observation of PG 0946+301. Therefore, no constraints could be put on the distance of the outflows from the central source (R).

COS enabled a significant breakthrough. Arav et al. (2013) analyzed two outflows, seen in COS data, of quasar HE 0238-1904. The width of both outflows was around 600 km s⁻¹, enabling the measurements of absorption troughs from O IV and O IV* that lead to an R determination. Accurate measurements of

N_{ion} from ions with a wide range of IP (O IV to Mg X) revealed the necessity of a two-phase photoionization solution similar to the one depicted in Figure 3. The combination of the large N_{H} of the VHP, the high velocity, and a large R yielded a large value of \dot{E}_k (see Table 2). Finn et al. (2014) used COS data of a narrow (full $\Delta v \sim 600 \text{ km s}^{-1}$), low-velocity outflow detected in quasar FBQS J0209-0438. They determined an R of 2000–6000 parsecs for different components of the outflow and showed the existence of two ionization phases.

Compared with the results of Arav et al. (2013), the work presented here advances our understanding of quasar outflows in several dimensions.

1. We show results for 13 outflows compared with the 2 analyzed in Arav et al. (2013), thus, (a) uncovering a wider outflow phenomenology, (b) enabling comparative analysis, and (c) putting the extrapolations of these results to quasar outflows, in general, on firmer ground. For example, the conclusion that most high-ionization outflows observed from the ground have a dominant VHP that is revealed by EUV500 observations (see Section 4.1).
2. The higher redshift of our targets let us measure troughs at shorter rest-frame wavelengths, which increase the robustness of our photoionization analysis, and especially the ability to probe the VHP of the outflows.
3. We have several cases of more than one n_e diagnostic for a given outflow (e.g., see Figure 3 in Paper III). The availability of two or more diagnostics minimize the probability of systematic issues that can lead to erroneous R determinations.

5.4. BAL Definition for the EUV500

Weymann et al. (1991) defined the criteria for a quasar absorption trough being classified as a BAL. The definition requires a continuous C IV absorption over $\Delta v \geq 2000 \text{ km s}^{-1}$ at $I \leq 0.9$ (where I is the normalized residual intensity) starting from at least -3000 km s^{-1} blueward of the emission line center. The BAL definition is focused on C IV since it usually produces the strongest absorption troughs observed long-ward of the Ly α forest. There is a 500 km s^{-1} velocity separation between the C IV doublets at 1548.19 and 1550.77 Å. Therefore, the BAL requirement for a C IV absorption trough from a single transition is $\Delta v \gtrsim 1500 \text{ km s}^{-1}$.

C IV absorption troughs are not covered in the EUV500. Therefore, we define a BAL in the EUV500 region as: continuous absorption with $I \leq 0.9$ over $\Delta v \gtrsim 1500 \text{ km s}^{-1}$, starting from at least -3000 km s^{-1} blueward of the emission line center, seen in the widest, uncontaminated absorption trough (in our sample, it is either Ne VIII 770.41 Å, Ne VIII 780.32 Å, or O V 629.73 Å). Mini-BALs (Hamann & Sabra 2004) are defined similarly with $1500 \gtrsim \Delta v \gtrsim 500 \text{ km s}^{-1}$. We note that the velocity separation between the Ne VIII doublet transitions is 3800 km s^{-1} . Therefore, if their absorption is self-blended, the outflow is clearly classified as a BAL.

6. Summary

We executed the first dedicated *HST*/COS survey of quasar outflows covering the diagnostic-rich 500–1050 Å rest-frame

(hereafter, EUV500) spectral region. This paper (Paper I) summarizes the main results of the survey and discuss their importance to various aspects of quasar research. A detailed analysis of the data is presented in Papers II–VI and VII (see Section 1).

Using 1 of the 13 outflows discussed here, we give an overview of how the scientific results are extracted from the data (see Section 3), including: the photoionization solution, number density, distance from the central source (R), and kinetic luminosity (\dot{E}_k).

In Section 4, we give a summary of the results from these investigations, including:

- (1) Measurements of the three most energetic outflows to date ($\dot{E}_k \geq 10^{46} \text{ erg s}^{-1}$), which can be the main agents for AGN feedback processes in the environments of the host galaxies.
- (2) All the outflows have a VHI component, similar to the one found in warm absorbers, which carries most of their kinetic luminosity. This detection suggests that all the high-ionization outflows detected from the ground also have a similar VHI component.
- (3) Of the 13 studied EUV500 outflows, 9 have $100 < R < 2000$ parsecs, 2 have $5 < R < 20$ parsecs, 1 has $0.05 < R < 50$ and in 1 cases, R cannot be determined.
- (4) One of the outflows has the largest velocity shift (1550 km s^{-1}) and acceleration (1.5 cm s^{-2}) measured to date. This outflow is physically similar to the fast X-ray outflow detected in quasar PG 1211+143.
- (5) These findings were partially enabled by the first detection of absorption troughs from previously unseen transitions of O IV*, O V*, Ar VI, Ne V*, Ne VI*, Ca IV, Ca V, Ca V*, Ca VI, Ca VII, Ca VII*, Ca VIII, and Ca VIII*.



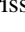
We discuss the many advantages of studying quasar outflows using EUV500 data compared to ground-based observations, including: the ability to measure the dominant VHP of the outflow, the ease and profound determination of the total N_{H} , and the ionization structure of the outflows. For the majority of EUV500 outflows, R can be determined, whereas it can be done in only a tiny fraction of ground-based spectra.

The VHP ionization parameter is similar to the lower ionization portion of the warm absorbers, which is seen in spectroscopic X-ray observations of Seyfert outflows. However, the warm absorbers reveal higher ionization phases through the detection of ions with much higher IP. It is probable that such phases occur also in quasar outflows but the EUV500 does not cover the needed spectral diagnostics.

N.A., X.X., and T.M. acknowledge support from NSF grant AST 1413319, as well as NASA STScI grants GO 14777, 14242, 14054, 14176, AR-15786, and NASA ADAP 48020. G.K. acknowledges support from NASA STScI grants GO 14777, 14242, 14054, and 14176; and NASA ADAP 48020.

Based on observations made with the NASA/ESA *Hubble Space Telescope*, and obtained from the data archive at the Space Telescope Science Institute. STScI is operated by the Association of Universities for Research in Astronomy, Inc. under NASA contract NAS5-26555. CHIANTI is a collaborative project involving George Mason University, the University of Michigan (USA), University of Cambridge (UK), and NASA Goddard Space Flight Center (USA).

ORCID iDs

Nahum Arav  <https://orcid.org/0000-0003-2991-4618>
 Xinfeng Xu  <https://orcid.org/0000-0002-9217-7051>
 Timothy Miller  <https://orcid.org/0000-0002-0730-2322>
 Gerard A. Kriss  <https://orcid.org/0000-0002-2180-8266>

References

- Anglés-Alcázar, D., Davé, R., Faucher-Giguère, C.-A., Özel, F., & Hopkins, P. F. 2017, *MNRAS*, **464**, 2840
- Aoki, K., Oyabu, S., Dunn, J. P., et al. 2011, *PASJ*, **63**, 457
- Arav, N., Borguet, B., Chamberlain, C., Edmonds, D., & Danforth, C. 2013, *MNRAS*, **436**, 3286
- Arav, N., Chamberlain, C., Kriss, G. A., et al. 2015, *A&A*, **577**, A37
- Arav, N., de Kool, M., Korista, K. T., et al. 2001, *ApJ*, **561**, 118
- Arav, N., Korista, K. T., de Kool, M., et al. 1999, *ApJ*, **516**, 27
- Arav, N., Liu, G., Xu, X., et al. 2018, *ApJ*, **857**, 60
- Barai, P., Proga, D., & Nagamine, K. 2011, *MNRAS*, **418**, 591
- Bautista, M. A., Dunn, J. P., Arav, N., et al. 2010, *ApJ*, **713**, 25
- Behar, E., Peretz, U., Kriss, G. A., et al. 2017, *A&A*, **601**, A17
- Blandford, R. D., & Begelman, M. C. 2004, *MNRAS*, **349**, 68
- Borguet, B. C. J., Arav, N., Edmonds, D., Chamberlain, C., & Benn, C. 2013, *ApJ*, **762**, 49
- Borguet, B. C. J., Edmonds, D., Arav, N., Benn, C., & Chamberlain, C. 2012a, *ApJ*, **758**, 69
- Borguet, B. C. J., Edmonds, D., Arav, N., Dunn, J., & Kriss, G. A. 2012b, *ApJ*, **751**, 107
- Chamberlain, C., Arav, N., & Benn, C. 2015, *MNRAS*, **450**, 1085
- Choi, E., Ostriker, J. P., Naab, T., et al. 2017, *ApJ*, **844**, 31
- Cicone, C., Brusa, M., Ramos Almeida, C., et al. 2018, *NatAs*, **2**, 176
- Ciotti, L., Ostriker, J. P., & Proga, D. 2009, *ApJ*, **699**, 89
- Dai, X., Shankar, F., & Sivakoff, G. R. 2008, *ApJ*, **672**, 108
- Danehar, A., Nowak, M. A., Lee, J. C., et al. 2018, *ApJ*, **853**, 165
- de Kool, M., Arav, N., Becker, R. H., et al. 2001, *ApJ*, **548**, 609
- de Kool, M., Becker, R. H., Arav, N., Gregg, M. D., & White, R. L. 2002, *ApJ*, **570**, 514
- Dere, K. P., Landi, E., Mason, H. E., et al. 1997, *A&AS*, **125**, 149
- Dubois, Y., Volonteri, M., & Silk, J. 2014, *MNRAS*, **440**, 1590
- Dunn, J. P., Arav, N., Aoki, K., et al. 2012, *ApJ*, **750**, 143
- Dunn, J. P., Bautista, M., Arav, N., et al. 2010, *ApJ*, **709**, 611
- Faucher-Giguère, C.-A., Quataert, E., & Murray, N. 2012, *MNRAS*, **420**, 1347
- Ferland, G. J., Chatzikos, M., Guzman, F., et al. 2017, *RMxAA*, **53**, 385
- Finn, C. W., Morris, S. L., Crighton, N. H. M., et al. 2014, *MNRAS*, **440**, 3317
- Ganguly, R., & Brotherton, M. S. 2008, *ApJ*, **672**, 102
- Green, J. C., Froning, C. S., Osterman, S., et al. 2012, *ApJ*, **744**, 60
- Grier, C. J., Brandt, W. N., Hall, P. B., et al. 2016, *ApJ*, **824**, 130
- Hamann, F., & Sabra, B. 2004, in ASP Conf. Ser. 311, AGN Physics with the Sloan Digital Sky Survey 311, ed. G. T. Richards & P. B. Hall (San Francisco, CA: ASP), 203
- Hamann, F. W., Barlow, T. A., Chaffee, F. C., Foltz, C. B., & Weymann, R. J. 2001, *ApJ*, **550**, 142
- Harrison, C. M., Costa, T., Tadhunter, C. N., et al. 2018, *NatAs*, **2**, 198
- Hewett, P. C., & Foltz, C. B. 2003, *AJ*, **125**, 1784
- Holczer, T., Behar, E., & Kaspi, S. 2007, *ApJ*, **663**, 799
- Hopkins, P. F., & Elvis, M. 2010, *MNRAS*, **401**, 7
- Hopkins, P. F., Murray, N., & Thompson, T. A. 2009, *MNRAS*, **398**, 303
- Kaasta, J. S., Kriss, G. A., Cappi, M., et al. 2014, *Sci*, **345**, 64
- Khalatyan, A., Cattaneo, A., Schramm, M., et al. 2008, *MNRAS*, **387**, 13
- Knigge, C., Scaringi, S., Goad, M. R., & Cottis, C. E. 2008, *MNRAS*, **386**, 1426
- Korista, K. T., Bautista, M. A., Arav, N., et al. 2008, *ApJ*, **688**, 108
- Korista, K. T., Weymann, R. J., Morris, S. L., et al. 1992, *ApJ*, **401**, 529
- Kriss, G. A., Lee, J. C., Danehar, A., et al. 2018, *ApJ*, **853**, 166
- Landi, E., Young, P. R., Dere, K. P., et al. 2013, *ApJ*, **763**, 86
- Leighly, K. M., Terndrup, D. M., Gallagher, S. C., Richards, G. T., & Dietrich, M. 2018, *ApJ*, **866**, 7
- Lucy, A. B., Leighly, K. M., Terndrup, D. M., Dietrich, M., & Gallagher, S. C. 2014, *ApJ*, **783**, 58
- Miller, T. R., Arav, N., Xu, X., et al. 2018, *ApJ*, **865**, 90
- Miller, T. R., Arav, N., Xu, X., Kriss, G. A., & Plesha, R. 2020a, *ApJS*, **247**, 39
- Miller, T. R., Arav, N., Xu, X., Kriss, G. A., & Plesha, R. 2020b, *ApJS*, **247**, 41
- Moe, M., Arav, N., Bautista, M. A., & Korista, K. T. 2009, *ApJ*, **706**, 525
- Murray, N., & Chiang, J. 1997, *ApJ*, **474**, 91
- Netzer, H., Kaspi, S., Behar, E., et al. 2003, *ApJ*, **599**, 933
- Osterbrock, D. E., & Ferland, G. J. 2006, *Astrophysics of Gaseous Nebulae and Active Galactic Nuclei* (2nd ed.; Sausalito, CA: Univ. Sci. Books)
- Ostriker, J. P., Choi, E., Ciotti, L., Novak, G. S., & Proga, D. 2010, *ApJ*, **722**, 642
- Peirani, S., Dubois, Y., Volonteri, M., et al. 2017, *MNRAS*, **472**, 2153
- Pettini, M., & Boksenberg, A. 1986, *ESA Spec. Publ.*, **263**, 627
- Pounds, K. A., Lobban, A., Reeves, J. N., & Vaughan, S. 2016a, *AN*, **337**, 518
- Pounds, K. A., Lobban, A., Reeves, J. N., Vaughan, S., & Costa, M. 2016b, *MNRAS*, **459**, 4389
- Rosas-Guevara, Y. M., Bower, R. G., Schaye, J., et al. 2015, *MNRAS*, **454**, 1038
- Scannapieco, E., & Oh, S. P. 2004, *ApJ*, **608**, 62
- Schaye, J., Crain, R. A., Bower, R. G., et al. 2015, *MNRAS*, **446**, 521
- Silk, J., & Rees, M. J. 1998, *A&A*, **331**, L1
- Steenbrugge, K. C., Kaastra, J. S., Crenshaw, D. M., et al. 2005, *A&A*, **434**, 569
- Taylor, P., & Kobayashi, C. 2015, *MNRAS*, **452**, L59
- Telfer, R. C., Kriss, G. A., Zheng, W., Davidsen, A. F., & Green, R. F. 1998, *ApJ*, **509**, 132
- Thompson, T. A., Fabian, A. C., Quataert, E., et al. 2015, *MNRAS*, **449**, 147
- Tornatore, L., Borgani, S., Viel, M., & Springel, V. 2010, *MNRAS*, **402**, 1911
- Volonteri, M., Dubois, Y., Pichon, C., & Devriendt, J. 2016, *MNRAS*, **460**, 2979
- Weymann, R. J., Morris, S. L., Foltz, C. B., & Hewett, P. C. 1991, *ApJ*, **373**, 23
- Wright, E. L. 2006, *PASP*, **118**, 1711
- Xu, X., Arav, N., Miller, T., & Benn, C. 2018, *ApJ*, **858**, 39
- Xu, X., Arav, N., Miller, T., & Benn, C. 2019, *ApJ*, **876**, 105
- Xu, X., Arav, N., Miller, T., Kriss, G. A., & Plesha, R. 2020a, *ApJS*, **247**, 38
- Xu, X., Arav, N., Miller, T., Kriss, G. A., & Plesha, R. 2020b, *ApJS*, **247**, 40
- Xu, X., Arav, N., Miller, T., Kriss, G. A., & Plesha, R. 2020c, *ApJS*, **247**, 42
- Yuan, F., Yoon, D., Li, Y.-P., et al. 2018, *ApJ*, **857**, 121
- Zakamska, N. L., & Greene, J. E. 2014, *MNRAS*, **442**, 784
- Zubovas, K., & King, A. R. 2014, *MNRAS*, **439**, 400